Editors' Suggestion

Field effect enhancement in buffered quantum nanowire networks

Filip Krizek,[1,*] Joachim E. Sestoft,[1,*] Pavel Aseev,[2,*] Sara Marti-Sanchez,[3] Saulius Vaitiekėnas,[1] Lucas Casparis,[1] Sabbir A. Khan,[1] Yu Liu,[1] Tomaš Stankevič,[1] Alexander M. Whiticar,[1] Alexandra Fursina,[4] Frenk Boekhout,[5] Rene Koops,[5] Emanuele Uccelli,[5] Leo P. Kouwenhoven,[2,4] Charles M. Marcus,[1] Jordi Arbiol,[3,6] and Peter Krogstrup[1,†]

[1]*Center for Quantum Devices and Station Q Copenhagen, Niels Bohr Institute, University of Copenhagen, 2100 Copenhagen, Denmark*
[2]*QuTech and Kavli Institute of Nanoscience, Delft University of Technology, 2600 GA Delft, The Netherlands*
[3]*Catalan Institute of Nanoscience and Nanotechnology (ICN2), CSIC and BIST, Campus UAB, Bellaterra, Barcelona, Catalonia, Spain*
[4]*Microsoft Station Q, Delft University of Technology, 2600 GA Delft, The Netherlands*
[5]*QuTech and Netherlands Organization for Applied Scientific Research (TNO), Stieltjesweg 1, 2628 CK Delft, The Netherlands*
[6]*ICREA, Passeig de Lluís Companys 23, 08010 Barcelona, Catalonia, Spain*

(Received 18 April 2018; published 7 September 2018)

III–V semiconductor nanowires have shown great potential in various quantum transport experiments. However, realizing a scalable high-quality nanowire-based platform that could lead to quantum information applications has been challenging. Here, we study the potential of selective area growth by molecular beam epitaxy of InAs nanowire networks grown on GaAs-based buffer layers, where Sb is used as a surfactant. The buffered geometry allows for substantial elastic strain relaxation and a strong enhancement of field effect mobility. We show that the networks possess strong spin-orbit interaction and long phase-coherence lengths with a temperature dependence indicating ballistic transport. With these findings, and the compatibility of the growth method with hybrid epitaxy, we conclude that the material platform fulfills the requirements for a wide range of quantum experiments and applications.

DOI: 10.1103/PhysRevMaterials.2.093401

I. INTRODUCTION

Material science plays a key role in quantum computing research. Long quantum state lifetimes—the fundamental prerequisite for realizing quantum computers—rely on the ability to produce materials with high purity and structural quality. Together with the requirements of scalability and reproducibility, these properties are what mainly defines the challenges of material science in quantum computing today. Proposals for topological quantum computing [1–3], which are based on hybrid semiconductor-superconductor nanowire (NW) networks, are being pursued by numerous research groups and have ignited intense research efforts on hybrid epitaxy [4–8]. NW scalability is tightly related to the semiconductor growth approach. Top-down lithography has been used to define NWs in two-dimensional layers [5,9] and a variety of methods have been pursued for alignment and positioning of bottom-up vapor-liquid-solid (VLS)-grown NWs, such as dielectrophoresis techniques [10], nanoscale combing [11], and magnetic aligning of NWs [12]. Despite these developments, large-scale synthesis of bottom-up grown high-mobility NW networks that are compatible with epitaxial interwire connections and semiconductor/superconductor epitaxy has still not been realized. To realize the epitaxial connections, a lot of effort has been put into the growth of branched NWs via the VLS method [8,13–15]. A scalable approach was developed in Refs. [16,17] using template-assisted growth of in-plane NW networks [18]. Nonetheless, this approach is not yet compatible with superconductor epitaxy. An alternative scalable approach is to use lithographically defined openings in a mask on a crystalline substrate. This method is referred to as selective area growth (SAG) and has until recently been used mainly in conjunction with metal organic chemical vapor deposition [19,20], metal organic vapor phase epitaxy [21,22], chemical beam epitaxy, and metal organic molecular beam epitaxy (chemical beam epitaxy) [23–26]. In contrast to molecular beam epitaxy (MBE), the dissociation kinetics of the chemical precursors in these methods enhance the growth selectivity on masked substrates by expanding the growth parameter window, but typically at a cost of crystal purity. Even though the initial work was reported about 30 years ago [27–30], only the recent promising results reported in Refs. [31–35] have renewed the interest in SAG by MBE.

In this work, we present selective area growth of InAs NW networks by MBE, which are grown either on GaAs-based buffer layers or directly on semi-insulating InP and GaAs substrates. We demonstrate growth of lithographically designed NW networks with well-defined junctions, where the faceting depends on the mask alignment to the crystal orientation of the substrate. We selectively grow Sb-dilute GaAs buffer layers with flat top facets that protrude out of the substrate plane and allow for significant elastic strain relaxation of the InAs. The improved interface quality results in an enhanced field effect response close to conductance pinch-off. In addition, magnetoconductance experiments show strong spin-orbit coupling and phase coherence where the temperature dependence indicates ballistic transport. Therefore, the compatibility of the SAG NW platform with the growth of epitaxial

*These authors contributed equally to this work.
†krogstrup@nbi.dk

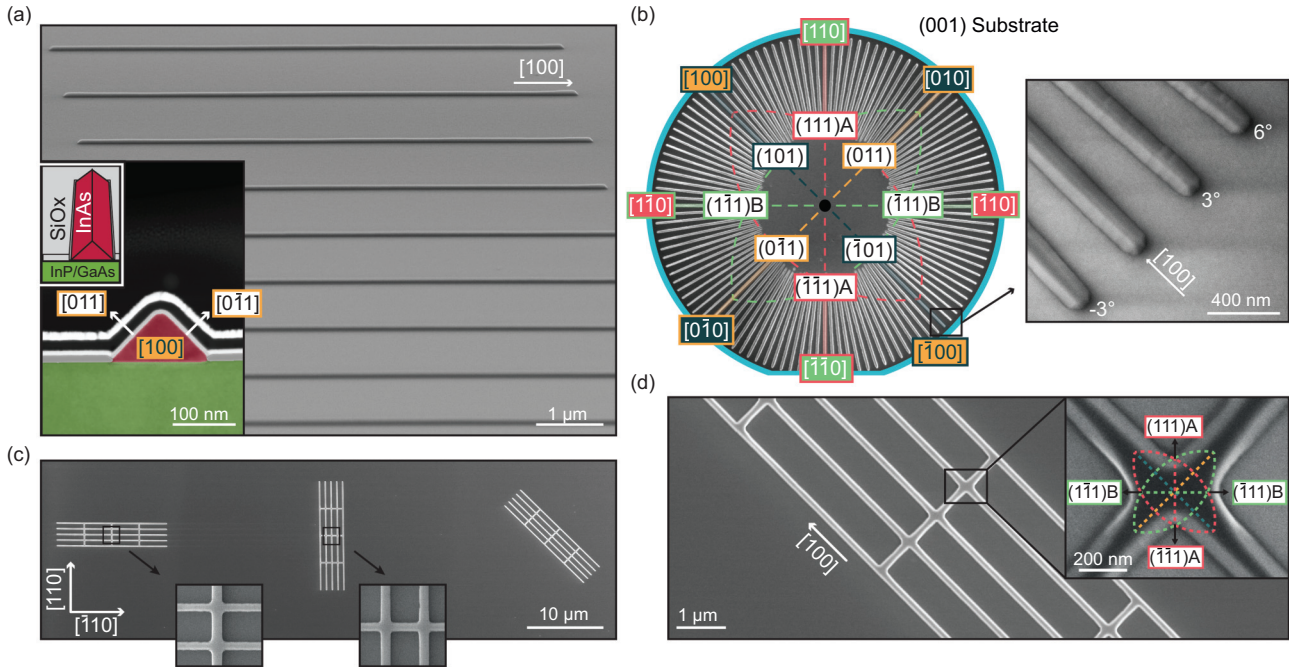

FIG. 1. (a) SEM micrograph of 10-μm-long [100] InAs NWs grown on InP (001) with a SiO_x mask. Inset shows a HAADF-STEM cross-section image of a NW, where the orientation and faceting is color correlated to the stereographic projection in (b). (b) Stereographic projection including the high-symmetry orientations of a [100] substrate, where the perimeter corresponds to in-plane NW directions (box fill color), with the facets normal to the NW given by the perpendicular orientations (corresponding border color). The graphics overlay an SEM micrograph of NWs selectively grown at increments of 3°. Zoom-in shows a [100] NW grown next to off-axis NWs with roughened and vicinal faceting. (c) SEM micrographs of three NW networks aligned along the [110], [1$\bar{1}$0], and [100] directions. (d) SEM micrograph of [100]/[010] NW network junctions. Zoom-in shows how the crystal symmetry results in twofold-symmetric junctions indicated by the polar (111)A and (111)B facets.

superconductors on selected facets [4] demonstrates its potential for large-scale applications in the field of gateable superconducting electronics (see Supplemental Material S1 [36] and Ref. [37] for details).

II. SCALABLE NANOWIRE NETWORKS

The InAs NWs are grown on semi-insulating (001) InP and GaAs substrates covered with thin dielectric masks at $T = 500$°C (pyrometer temperature) with a corresponding planar growth rate of ~0.1 μm/h for InP substrates and 0.26 μm/h for GaAs substrates with a total calibrated V-III ratio of ~10. The mask openings were defined by electron beam lithography (EBL) and selective etching. The patterns used for the characterized devices range from 100 to 350 nm in width and several micrometers in length with a pitch varying between 1 and 10 μm. See Supplemental Material S2 for details [36].

The substrates become fully insulating at low temperatures and are therefore suitable for as-grown device fabrication and transport experiments directly on the growth substrate. The scanning electron microscope (SEM) micrograph in Fig. 1(a) shows an array of InAs NWs oriented along the [100] direction on a (001) Fe-doped InP substrate. For SAG of InAs NWs on GaAs substrates, see Supplemental Material S3 [36]. The NWs exhibit smooth (011) and (0$\bar{1}$1) facets, as shown in the colored high-angle annular dark-field scanning transmission electron microscope (HAADF-STEM) image in the Fig. 1(a) inset. The uniformity of individual NW facets depends on the growth conditions [32,34] and the quality of the prepatterned substrate. Moreover, uniform, high-symmetry facets were found only on NWs oriented along the high-symmetry [100], [010], [1$\bar{1}$0], and [110] crystal directions, as illustrated in the stereographic projection in Fig. 1(b). For instance, a NW oriented along the [100] direction has {0$\bar{1}$1} family facets due to local cusps in surface energy. Even though the roughness of the NWs depends on growth conditions, a slight misalignment with respect to the high-symmetry crystal orientation causes vicinal faceting, as shown in the zoom-in of Fig. 1(b). Consequently, there are constraints on the in-plane directions, which set the overall symmetry and design of the NW networks. In the case of networks grown on (001) substrates, there are eight high-symmetry in-plane directions (indicated on the perimeter of the stereographic projection). As a result, one junction can be connected to eight NWs. There are two families of networks on (001) substrates consisting of perpendicularly oriented NWs, the ⟨110⟩/⟨1$\bar{1}$0⟩ type and the ⟨100⟩/⟨010⟩ type [see Fig. 1(c)]. At given growth conditions, both types of junctions exhibit a fourfold-symmetric morphology for short growth times. However, as the NWs grow thicker, the junctions tend to become twofold symmetric [see Fig. 1(d)]. In the case of the ⟨110⟩/⟨1$\bar{1}$0⟩ junction the symmetry breaking is related to the growth kinetics, where the difference in adatom diffusion lengths along the [110] and [1$\bar{1}$0] directions causes the material to incorporate more easily along the [110] direction [38]. At the given growth time and conditions, the ⟨110⟩/⟨1$\bar{1}$0⟩ NW

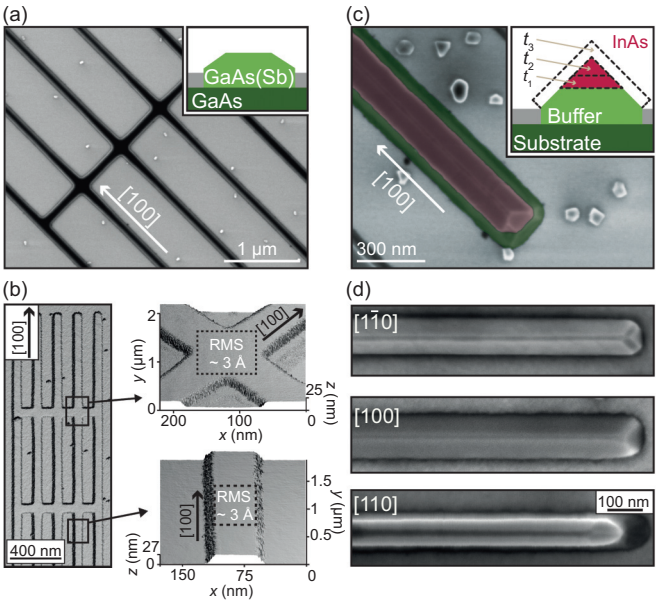

FIG. 2. (a) SEM micrograph of a selectively grown GaAs(Sb) NW network. (b) AFM scans showing flat (001) top facets of GaAs(Sb) networks aligned along the [100]/[010] directions. Zoom-ins on highlighted areas show the extracted roughness of the top facet of a junction and a straight NW. (c) SEM micrograph of InAs NWs selectively grown on the top facet of the buffer. Inset shows the InAs NW morphology evolution with growth time, t_{1-3}. (d) SEM micrographs of InAs NWs grown on the buffer in the three highest in-plane symmetry directions. The cross-section shapes of NWs from the same growth are presented in Figs. 3(a)–3(c).

junctions maintain a nontapered fourfoldlike morphology as seen in the inset of Fig. 1(c). In the ⟨100⟩/⟨010⟩ case, the symmetry breaking appears earlier, likely due to the different polarity of faceting of the two orientations, as indicated in Fig. 1(d).

III. BUFFERED NANOWIRES

We find that top-gated InAs NWs grown directly on nonbuffered InP or GaAs substrates generally display a weak field effect response close to the conductance pinch-off region. This is most likely related to the NW/substrate interface. To enhance the electrical properties of the NWs, we focus on improving the quality of the interface and turn our attention to $GaAs_{1-x}Sb_x$ buffers where the lattice matching can be tuned from GaAs to InAs by changing the composition, x.

The GaAs(Sb) buffer was grown on undoped (001) GaAs substrates at 615°C, at a growth rate of 0.1 μm/h, total V-III ratio of ∼20, and As_2/Sb_{2+4} ratio of ∼7. The InAs on top of the buffer was grown at 500°C with a corresponding planar growth rate of 0.1 μm/h and a total V-III ratio of ∼10.

In Fig. 2(a) we show an SEM micrograph of a GaAs(Sb) buffer NW network grown on a semi-insulating (001) GaAs substrate. We find that the buffer layer has flat (001) top facets, with a root-mean-square (rms) roughness of ∼3 Å. The roughness is uniform across the whole wafer as shown on both single NWs and within the junctions in Fig. 2(b) (see Supplemental Material S4 [36] for analysis of the other NW orientations).

We emphasize that the flatness of the buffer is a crucial step towards obtaining a low-disorder interface to the InAs transport channel. Compositional analysis performed by electron-energy-loss spectroscopy (EELS) and energy-dispersive x-ray spectroscopy (EDX) reveals a very low fraction of Sb (close to the detection limit of ∼2%). This is lower than the calibrated flux ratios, which would predict ∼7% if the incorporation rates of As and Sb were equal. The low incorporation efficiency of Sb is consistent with previous reports [39,40]. Despite the low Sb incorporation (which has a negligible effect on the lattice constant), the surfactant properties of Sb play an important role in the growth kinetics and promote a smooth buffer growth. The effect is shown in Supplemental Material S4 [36].

In Fig. 2(c) we show that InAs can be grown selectively on the top facet of the GaAs(Sb) buffer. Both the buffer and InAs were grown close to the "lower bound" of the selective window where material starts to stick on the dielectric mask. The lower bound is apparent from material deposition on the oxide mask, which takes place when the temperature is too low or the fluxes too high. In contrast, the "upper bound" of the selective window is apparent when the growth rate in the selective areas becomes negative, which occurs when the temperature is too high or the fluxes too low. The critical fluxes that bound the growth window depend exponentially on temperature as well as on the specific dielectric used as the mask material. In this work, we generally find that the NW morphology appears smoother and more uniform closer to the lower bound of the selective growth window.

The morphology of the NWs grown on the buffer is highly dependent on the growth time and the width of the buffer top facet. In the inset of Fig. 2(c) we show an illustration of what a predicted evolution of the growth would look like if it was thermodynamically driven, i.e., able to reach the lowest free energy (or equilibrium shape) for any given volume. The equilibrium shape of a crystal results from minimizing its anisotropic surface free energy under the constraint of constant volume. If there are additional constraints, such as a mask opening into which the crystal is confined to, then the equilibrium shape will depend on its volume. Assuming that the cross-section shape of the SAG NWs are equilibrium shapes, the NWs will most likely first grow solely on the top facets of the buffer until a fully faceted shape is reached, as illustrated in the inset of Fig. 2(c) at growth time t_2. This particular equilibrium shape is also of special interest for realization of high-quality SAG NWs, for reasons discussed below. It is clear that the ratio of the buffer to NW growth time affects the shape and dimensions of the NW structures, and understanding the detailed processes, whether in thermodynamical or kinetically driven regimes, will be the subject of ongoing studies. In Fig. 2(d) we show that uniform and continuous buffered NWs can be grown in all three high-symmetry orientations.

Control over the width of the mask opening becomes difficult for features below 90 nm when wet etching is used. However, implementation of the buffer layer, where the top-facet width is decreasing with growth time, also provides an *in situ* method for tuning the InAs NW width. This opens up the possibility of engineering thinner NWs that are not in contact with either the oxide mask or the processed mask opening (see Supplemental Material S5 [36].

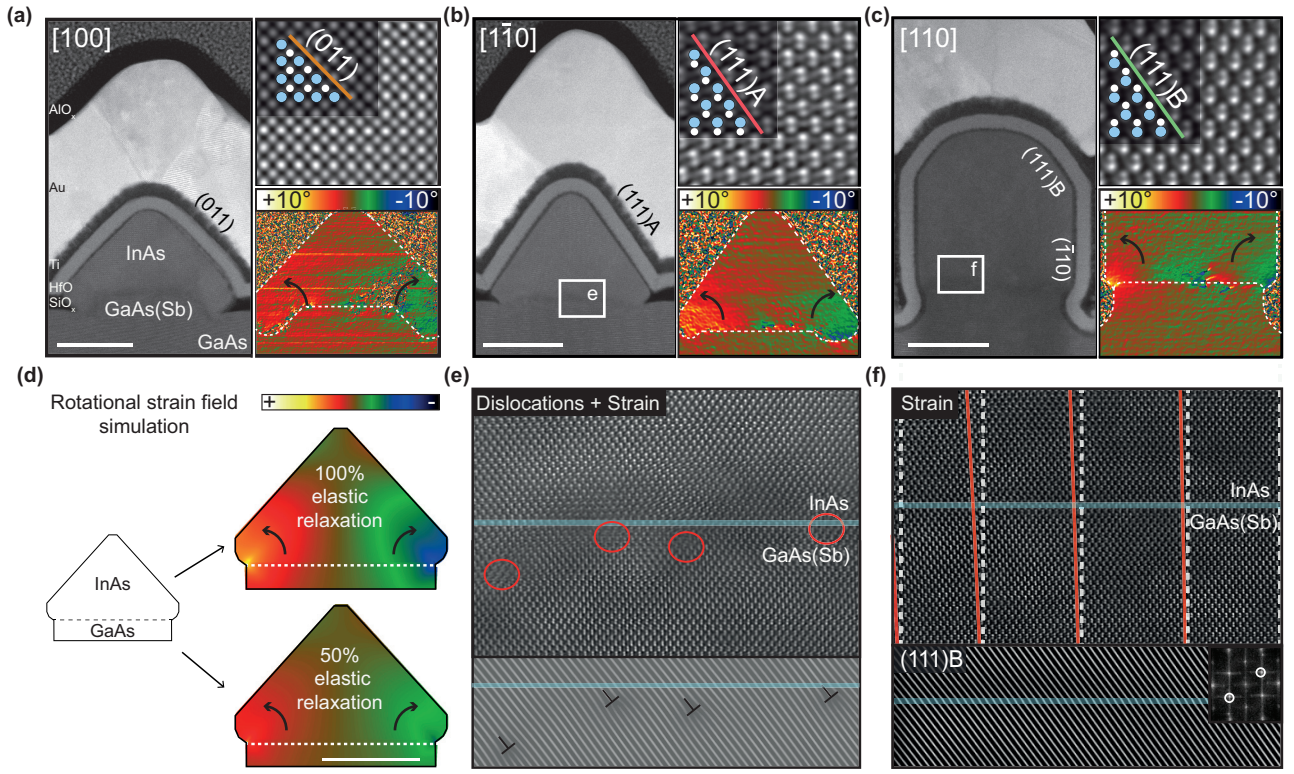

FIG. 3. Cross-section TEM micrographs of top-gated devices with InAs NWs grown on top of GaAs(Sb) buffer layers along the (a) [100], (b) [1$\bar{1}$0], and (c) [110] orientations. Top right insets are cross-sectional HAADF-STEM images of the InAs NW segments with pure crystalline structures, where the illustrated high-symmetry plane highlights the related facet polarity (As atoms, white; In atoms, blue). Bottom right insets show geometric phase analysis (GPA) rotational maps around the (111) planes. Scale bars are 50 nm. (d) GPA rotational map simulation for a [100]-oriented buffered NW showing elastic strain relaxation profiles. Scale bar is 50 nm. (e) Atomic-resolution aberration-corrected HAADF-STEM micrograph of the interface indicated in (b) showing misfit dislocations and strain. The bottom panel is the same image after fast Fourier transform (FFT) filtering, with a highlighted aperiodic misfit dislocation array. The blue line indicates the interface. (f) Atomic-resolution aberration-corrected HAADF-STEM micrograph of the interface indicated in (c) showing no misfit dislocations and pronounced strain as indicated by the white dashed lines (no strain) and red line (the actual plane displacement). The bottom panel is the same image after FFT filtering, with no visible misfit dislocations.

IV. ELASTIC STRAIN RELAXATION

Atomic resolution and aberration corrected HAADF-STEM characterization was performed on cross-section cuts of top-gated NW devices. Figure 3 shows three corresponding cross-section shapes of single [100], [1$\bar{1}$0], and [110] InAs NWs grown on GaAs(Sb) buffer [Figs. 3(a)–3(c)]. The NWs originate from the same growth and same region of the substrate with at least 10 μm separation from other structures. The corresponding planar growth thickness was 50 nm for the GaAs buffer and 35 nm for the InAs. However, as apparent in Fig. 3(c), the NW volume can exceed the nominal thickness. This means that the atomic beams impinging on the oxide can contribute to the growth in the selective areas, via surface diffusion. Moreover, the reasons for the differences in growth rates between the different orientations can be of both thermodynamic and kinetic origin, i.e., due to differences in surface energies and activation barriers for diffusion and incorporation. Under the given mass transport conditions, the dynamics of the shape evolution is thermodynamically driven by the excess chemical potential of the crystal phase, which can be described by relevant shape parameters [38]. In the case of continuous and uniform SAG NWs, that are constrained to the selective area, the relevant shape parameters are only the side-facet sizes (and their relative surface energies). However, the differences in adatom kinetics between the orientations could also play an important role and future studies will be needed to identify the main mechanisms for the differences in growth observed between the orientations.

The HAADF-STEM micrographs show that there are no threading dislocations running through the NWs (as also reported in Ref. [34]) and that the bulk structure is single crystalline for all three NW orientations. The highlighted facet planes correspond to the stereographic projection shown in Fig. 1(b) which will also determine the corresponding NW shape. We further note that the three different types of facets, nonpolar, A-polar, and B-polar, are likely to have different electron affinities and provide additional band alignment options when optimizing contact to superconductors or metals.

The relative lattice mismatches between the InAs NW and the InP or GaAs substrates are 3% and 7%, respectively. As shown in Supplemental Material S6 [36], when growing directly on InP substrates, without a buffer layer, the lattice mismatch to InAs is fully compensated by relaxation at the interface via periodic arrays of misfit dislocations. That results in an abrupt change of the lattice spacing at the substrate/NW

interface. The situation is different for the buffered NWs, where the buffer protrudes out of the substrate plane. Consequently, the InAs NWs have significantly more freedom to make the elastic rotation needed to relax to its equilibrium lattice parameter without introducing dislocations. This effect is observed on all analyzed buffered GaAs(Sb)/InAs interfaces, which is apparent from the gradual change in lattice constant and significantly lower density of misfit dislocations.

The lower right insets of Figs. 3(a)–3(c) show the geometric phase analysis (GPA) of the rotational displacement of the (111) crystal planes. The rotation is a sign of a gradual and partially elastic change of the lattice spacing from GaAs to InAs. An average value for rotation in these structures is on the order of 3° (left side) to −3° (right side). This signature of elastic strain relaxation is illustrated in a qualitative simulation of the rotational displacement field of a fully strained and partially strained GaAs/InAs NW in Fig. 3(d) (see Methods in the Supplemental Material [36] for simulation details). Figure 3(e) shows an image of the GaAs(Sb)/InAs interface of the [1$\bar{1}$0] NW, where nonperiodic misfit dislocations (clearly visible after Fourier filtering) indicate partial plastic strain relaxation. Figure 3(f) shows a zoom-in on a GaAs(Sb)/InAs dislocation-free interface region of the [110] NW, where the rotation of the (111) crystal planes peaks at 4.5°. Here, the interface is nearly dislocation free except for a small region close to the middle of the NW, which means that the NW is close to being fully elastically strain relaxed in the transverse component. The results of the GPA show that most of the elastic strain is released within ∼20 nm around the interface, where the lattice constant changes from 5.71 to 6.06 Å with a mean dilatation of 6.1% (see Supplemental Material S6 [36]).

We note that the strain relaxation mechanism is similar to that in axial heterostructures of free-standing VLS-grown NWs [41] and to the elastic rotation previously observed in InGaN/GaN [42] and InAs/InSb [43,44] and also for larger selectively grown structures [45]. This very important trend opens new possibilities for engineering of elastically strain relaxed SAG NW structures and clearly shows the potential and importance of growth on the top facet of SAG buffers. This is also apparent from the fact that the InAs NW on the GaAs(Sb) buffer has fewer misfit dislocations than in the case of direct growth on the InP substrate, which has a lower lattice mismatch to InAs (see Supplemental Material S6 [36]).

V. FIELD EFFECT ENHANCEMENT

For computing applications—classical or quantum—the device performance depends on the ability to effectively gate and pinch off conductance. Since back-gating can be challenging on semi-insulating substrates we use top gates for the carrier density control. Figure 4(a) shows a false-colored device lithographically similar to the characterized devices, where only gate width, W, is varied. Figure 4(b) shows conductance, G, as a function of gate voltage, V_g, for an InAs NW grown on the nonbuffered GaAs substrate. The charge carrier density is not fully depleted even for very negative V_g and the down and up gate traces are highly hysteretic (see Supplemental Material S7 [36]). This is a general trend for the nonbuffered NWs we measured (on both GaAs and InP). The schematics depict two characteristic gate voltage regions with different slopes

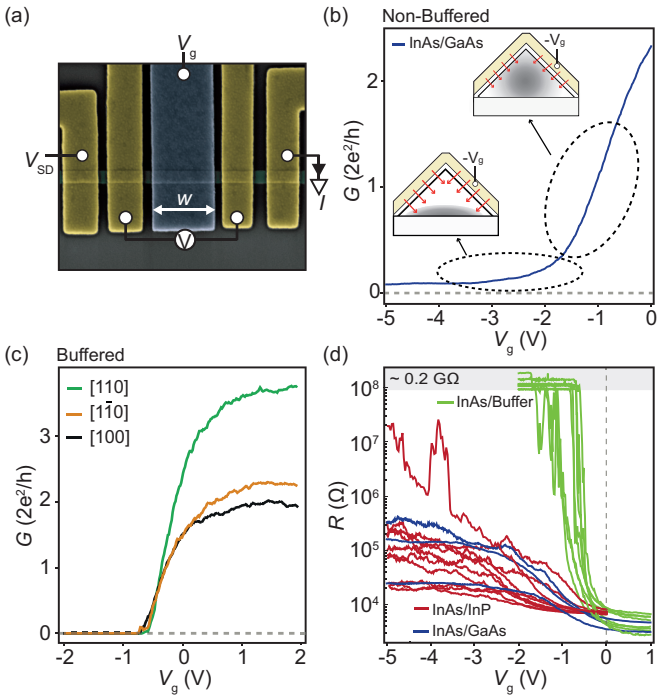

FIG. 4. (a) False-colored SEM micrograph of a typical top-gated four-probe NW device. Yellow, Ti/Au contacts; blue, gates; grey, InAs NW; V_{SD}, bias voltage; I, measured current; V_g, gate voltage controlling the chemical potential; W, gate width. (b) Conductance, G, as a function of V_g, for InAs grown on a GaAs substrate. Sketches illustrate the carrier density distribution as a function of V_g. The two regimes correspond to transport residing in the whole InAs transport channel (lower negative V_g) and at the InAs/substrate interface (more negative V_g). (c) Conductance as a function of V_g for InAs NWs grown on the GaAs(Sb) buffer along the [110], [1$\bar{1}$0], and [100] directions. (d) Resistance, R, as a function of V_g for multiple NW samples grown directly on InP, GaAs, and the buffer layer.

of conductance. Due to the top-gate geometry, the carriers in the NW will first be depleted in the top part of the NW, corresponding to the region with the highest slope in Fig. 4(b). As more negative V_g is applied, the carrier density moves towards the NW/substrate interface. The transconductance depends on the quality of the semiconductor crystal. This allows for a qualitative evaluation of the NW/substrate and NW/buffer interfaces. Therefore, the interface is mainly probed at more negative gate voltages [as indicated by the sketch in Fig. 4(b)]. For NWs grown directly on the substrate, the bottom interface appears to have a significantly lower field effect mobility. The low interfacial quality can be caused by the presence of misfit dislocations, potential impurities, midgap states induced by thermal deoxidation [46], and roughness originating from the etching process. Additionally, the pregrowth annealing step used to remove the native oxide is likely to play an important role [47].

Figure 4(c) shows examples of G as a function of V_g for three InAs NWs grown on the buffer layer in the three high-symmetry crystal orientations. The measurements on buffered NWs show a high degree of reproducibility, as all the NWs measured on this growth pinch off within a window of ∼250 mV. In contrast to the nonbuffered NWs in Fig. 4(b),

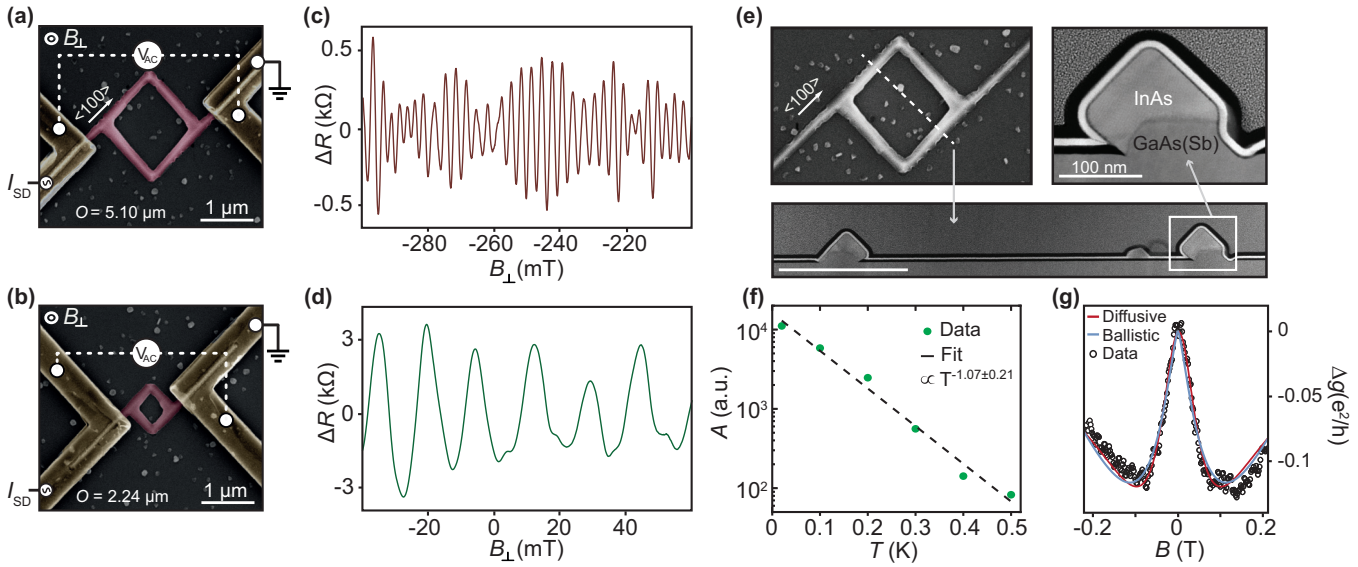

FIG. 5. (a, b) False-colored SEM micrographs of the four-probe NW loop devices. (c, d) Change in resistance, ΔR, as a function of perpendicular magnetic field, $B_\perp$, over a 100-mT range showing electron phase interference oscillations for the larger and smaller loop, respectively. (e) Overview SEM and cross-section HAADF-STEM micrographs of the Aharonov-Bohm loop structure showing the asymmetric cross-section. The dashed white line indicates where the cross-section was made. Scale bar corresponds to 500 nm. (f) Integrated FFT of the oscillations plotted as a function of temperature. The fitted line corresponds to the linear fit of the h/e oscillation amplitudes and yields $l_\phi \sim 13\ \mu$m. (g) Offset magnetoconductance traces showing WAL effects around $B = 0$, for the diffusive and ballistic regime WAL expression fit.

there is no apparent difference in transconductance between the bulk and the interface gate regions, indicating that the quality of the interfaces is significantly improved. In Fig. 4(d) we show data from multiple buffered and the nonbuffered NWs of comparable dimensions. Here, the gate-dependent resistance is shown for different high-symmetry NW orientations, with W varying from 250 nm to 2.5 μm. On the logarithmic scale, it is apparent that the conductance is not completely pinched off in any of the nonbuffered NW devices (within reasonable gate range and with the selected NW volumes). In addition the nonbuffered NWs show more pronounced hysteresis in down/up gate sweeps than the buffered NWs (see Supplemental Material S7 [36]).

Even though the field effect mobility depends on the gate voltage V_g, range, and carrier density distribution, we use a full fit to the conductance as a function of V_g to extract the mean mobility, as shown in Ref. [48]. For details of fitting and finite element modeling of the capacitance, see Supplemental Material S8 and S9 [36]. The average mean mobility measured on the buffered NWs is about $\bar{\mu} \sim 5600 \pm 1300\ \mathrm{cm}^2/(\mathrm{V\,s})$ with a maximum at $\sim$7600 $\mathrm{cm}^2/(\mathrm{V\,s})$ (extracted from 24 data sets: 6 buffered devices at 1, 2, 5, and 10 mV bias). More detailed finite element method modeling of the capacitances, including the detailed modeling of the specific cross-section shapes, is required for a more exact estimation and for comparison of different NWs and NW orientations. It is clear that the buffer layer significantly improves the transport characteristics of the NWs, regardless of their orientation or cross-section area.

VI. COHERENT QUANTUM TRANSPORT

We now turn our focus to the quantum transport properties, where quantum phase coherence, scattering length, and spin-orbit strength are important characteristics. To study the phase coherence we first fabricated two four-probe loop devices with a circumference of 5.1 μm and 2.24 μm for Aharonov-Bohm (AB)-type measurements as shown in Figs. 5(a) and 5(b), respectively. The resistance shows oscillations in perpendicular magnetic field, $B_\perp$, as seen in the 100 mT sweep range in Figs. 5(c) and 5(d). Magnetic fields on the order of 900 mT were applied along the [110] and [1$\bar{1}$0] in-plane substrate orientations in order to reduce weak antilocalization (WAL) effects and the aperiodic oscillating background was removed by Savitzky-Golay filtering [49]. The oscillation periods of $\sim$ 2.5 mT (large loop) and $\sim$14 mT (small loop) are in good agreement with the areas of the loops, given as $\sim h/(e \times \text{area})$. In Fig. 5(e) we show a cross-section TEM image of the loop, as indicated with the dashed line on the SEM image. The asymmetric shape of the InAs NWs on the GaAs(Sb) buffer is related to the growth mechanism of minimizing surface-to-volume ratio at the junction between the two high-symmetry orientations. We expect this effect to be suppressed with shorter growth time, in line with the discussion on the growth evolution above.

The phase-coherence length $l_\phi(T)$ can be extracted by fitting the temperature dependence of the AB oscillation amplitude, A, obtained from the Fourier spectra (see Supplemental Material S10 [36]). Assuming that the amplitude scales as $A(T) \propto \exp(-\frac{O}{l_\phi(T)})$, where O is the loop circumference [50], then the exponent m in $l_\phi(T) \propto T^{-m}$ can be determined. For the small loop we extract the exponent and the phase-coherence length by fitting to the logarithm of the amplitude, and get $m = 1.07 \pm 0.21$ and $l_\phi(20\ \mathrm{mK}) = 13 \pm 1\ \mu$m [see Fig. 5(f)]. It was not possible to obtain a reliable temperature dependence on the large loop due to charge noise switching. In the diffusive regime the temperature dependence of the coherence length in a loop-shaped structure follows $l_\phi \propto T^{-1/2}$, while in the ballistic

case with a weak coupling to the environment $l_\phi \propto T^{-1}$ as reported in Refs. [51–53]. This indicates that the small loop resides in the ballistic regime below ∼500 mK while the nonbuffered loop reported in Ref. [37] in the diffusive regime.

Characteristic length scales can also be extracted from WAL measurements on single NWs, where the coherence length depends on temperature as $l_\phi \propto T^{-1/3}$ [54–56]. The analytical WAL model can be used as a fitting model to extract a measure of phase-coherence length and spin-orbit length, but it depends on the cross-section confinement potential in the NW, including band bending. However, estimating the effective shape that goes into the derivation of an appropriate WAL formula is outside the scope of this work. Here we extract relative measures of the involved length scales using the typical assumption of a cylindrical cross section [57–59]. We fit both ballistic and diffusive models [59] to the data, as shown in Fig. 5(f). In both regimes, we extract a significantly smaller l_ϕ than from the AB experiment. The diffusive formula yields spin-orbit length, $l_{SO} \sim 85$ nm and $l_\phi \sim 210$ nm, where the best fit (based on standard deviation between model and the data) corresponds to the effective NW width $W_{eff} = 142$ nm. That is comparable to numbers extracted from similar measurements on VLS-grown InAs, InSb, and $InAs_{1-x}Sb_x$ NWs [7,59–62]. For the ballistic model, the elastic scattering length l_e goes into the model as an additional parameter. Here, we have fitted the ballistic formula for wide range of W_{eff} and l_e and found that the best fit yields $l_{SO} \sim 298$ nm and $l_\phi \sim 459$ nm for $l_e = 138$ nm and and $W_{eff} = 115$ nm. See Supplemental Material S11 [36] for details of the fitting procedure.

The extracted values of phase-coherence length significantly differ between the AB and WAL experiments. As the materials are almost identical, we believe that the reason is mainly due to differences in measured interference dephasing mechanisms [54], as well as the assumptions made for the particular formulas.

In conclusion, we show that selective area growth of high-quality InAs NW networks with well-defined junctions is feasible in MBE. The NWs can attain significant elastic strain relaxation when grown on top of flat selective-area-grown buffer layers, with significant improvement of the transport properties in terms of field effect response. Moreover, the material possesses promising quantum transport properties, e.g., strong spin-orbit coupling extracted from WAL and phase coherence demonstrated by AB experiments. We believe that these findings, combined with superconductor epitaxy [37], make this material platform an ideal large-scale architecture for quantum applications that are based on gateable superconducting electronics.

ACKNOWLEDGMENTS

The project was supported by Microsoft Station Q, the European Research Council (ERC) under Grant No. 716655 (HEMs-DAM), the European Union Horizon 2020 research and innovation program under the Marie Skłodowska-Curie Grant No. 722176, the Danish National Science Research Foundation, and the Villum Foundation. We thank Chris Palmstrøm, Philippe Caroff, Lucia Sorba, and Roman Lutchyn for fruitful discussions, and thank Claus B. Sørensen, Robert McNeil, Karthik Jambunathan, Keita Ohtani, and Shivendra Upadhyay for technical assistance in Copenhagen. S.M.S. acknowledges funding from "Programa Internacional de Becas 'la Caixa'-Severo Ochoa." J.A. and S.M.S. also acknowledge funding from Generalitat de Catalunya 2017 SGR 327. ICN2 acknowledges support from the Severo Ochoa Programme (MINECO, Grant No. SEV-2013-0295) and is funded by the CERCA Programme/Generalitat de Catalunya. Part of the present work has been performed in the framework of Universitat Autònoma de Barcelona Materials Science Ph.D. program. The HAADF-STEM microscopy was conducted in the Laboratorio de Microscopias Avanzadas at the Instituto de Nanociencia de Aragon-Universidad de Zaragoza. J.A. and S.M.S. thank them for offering access to their instruments and expertise.

[1] Y. Oreg, G. Refael, and F. von Oppen, Phys. Rev. Lett. **105**, 177002 (2010).
[2] R. M. Lutchyn, J. D. Sau, and S. Das Sarma, Phys. Rev. Lett. **105**, 077001 (2010).
[3] S. D. Sarma, M. Freedman, and C. Nayak, npj Quantum Inform. **1**, 15001 (2015).
[4] P. Krogstrup, N. Ziino, W. Chang, S. Albrecht, M. Madsen, E. Johnson, J. Nygård, C. Marcus, and T. Jespersen, Nat. Mater. **14**, 400 (2015).
[5] J. Shabani, M. Kjaergaard, H. J. Suominen, Y. Kim, F. Nichele, K. Pakrouski, T. Stankevic, R. M. Lutchyn, P. Krogstrup, R. Feidenhans'l, S. Kraemer, C. Nayak, M. Troyer, C. M. Marcus, and C. J. Palmstrøm, Phys. Rev. B **93**, 155402 (2016).
[6] J.-H. Kang, A. Grivnin, E. Bor, J. Reiner, N. Avraham, Y. Ronen, Y. Cohen, P. Kacman, H. Shtrikman, and H. Beidenkopf, Nano Lett. **17**, 7520 (2017).
[7] J. E. Sestoft, T. Kanne, A. N. Gejl, M. von Soosten, J. S. Yodh, D. Sherman, B. Tarasinski, M. Wimmer, E. Johnson, M. Deng *et al.*, Phys. Rev. Mater. **2**, 044202 (2018).
[8] S. Gazibegovic, D. Car, H. Zhang, S. C. Balk, J. A. Logan, M. W. de Moor, M. C. Cassidy, R. Schmits, D. Xu, G. Wang *et al.*, Nature (London) **548**, 434 (2017).
[9] F. Nichele, A. C. C. Drachmann, A. M. Whiticar, E. C. T. O'Farrell, H. J. Suominen, A. Fornieri, T. Wang, G. C. Gardner, C. Thomas, A. T. Hatke, P. Krogstrup, M. J. Manfra, K. Flensberg, and C. M. Marcus, Phys. Rev. Lett. **119**, 136803 (2017).
[10] E. M. Freer, O. Grachev, X. Duan, S. Martin, and D. P. Stumbo, Nat. Nanotechnol. **5**, 525 (2010).
[11] J. Yao, H. Yan, and C. M. Lieber, Nat. Nanotechnol. **8**, 329 (2013).
[12] C. M. Hangarter and N. V. Myung, Chem. Mater. **17**, 1320 (2005).
[13] J.-H. Kang, Y. Cohen, Y. Ronen, M. Heiblum, R. Buczko, P. Kacman, R. Popovitz-Biro, and H. Shtrikman, Nano Lett. **13**, 5190 (2013).
[14] D. Car, J. Wang, M. A. Verheijen, E. P. Bakkers, and S. R. Plissard, Adv. Mater. **26**, 4875 (2014).

[15] F. Krizek, T. Kanne, D. Razmadze, E. Johnson, J. Nygård, C. M. Marcus, and P. Krogstrup, Nano Lett. **17**, 6090 (2017).

[16] M. Borg, H. Schmid, K. E. Moselund, D. Cutaia, and H. Riel, J. Appl. Phys. **117**, 144303 (2015).

[17] H. Schmid, M. Borg, K. Moselund, L. Gignac, C. Breslin, J. Bruley, D. Cutaia, and H. Riel, Appl. Phys. Lett. **106**, 233101 (2015).

[18] J. Gooth, M. Borg, H. Schmid, V. Schaller, S. Wirths, K. Moselund, M. Luisier, S. Karg, and H. Riel, Nano Lett. **17**, 2596 (2017).

[19] B. D. Joyce and J. A. Baldrey, Nature **195**, 485 (1962).

[20] D. W. Shaw, J. Electrochem. Soc. **113**, 904 (1966).

[21] Y. Kato, S. Kitamura, K. Hiramatsu, and N. Sawaki, J. Cryst. Growth **144**, 133 (1994).

[22] P. Mohan, F. Nakajima, M. Akabori, J. Motohisa, and T. Fukui, Appl. Phys. Lett. **83**, 689 (2003).

[23] N. Vodjdani, A. Lemarchand, and H. Paradan, J. Phys. Colloq. **43**, C5 (1982).

[24] E. Tokumitsu, Y. Kudou, M. Konagai, and K. Takahashi, J. Appl. Phys. **55**, 3163 (1984).

[25] D. Andrews, M. Rejman-Greene, B. Wakefield, and G. Davies, J. Cryst. Growth **95**, 167 (1989).

[26] N. Furuhata and A. Okamoto, J. Cryst. Growth **112**, 1 (1991).

[27] S. Yokoyama, J. Oogi, D. Yui, and M. Kawabe, J. Cryst. Growth **95**, 32 (1989).

[28] A. Okamoto and K. Ohata, Appl. Phys. Lett. **51**, 1512 (1987).

[29] T. Sugaya, Y. Okada, and M. Kawabe, Jpn. J. Appl. Phys. **31**, L713 (1992).

[30] N. Kuroda, S. Sugou, T. Sasaki, and M. Kitamura, Jpn. J. Appl. Phys. **32**, L1627 (1993).

[31] L. Desplanque, X. Han, M. Fahed, V. K. Chinni, D. Troadec, M.-P. Chauvat, P. Ruterana, and X. Wallart, in *26th International Conference on Indium Phosphide and Related Materials (IPRM)* (IEEE, New York, 2014), pp. 1–2.

[32] L. Desplanque, M. Fahed, X. Han, V. Chinni, D. Troadec, M. Chauvat, P. Ruterana, and X. Wallart, Nanotechnology **25**, 465302 (2014).

[33] G. Tutuncuoglu, M. de La Mata, D. Deiana, H. Potts, F. Matteini, J. Arbiol, and A. F. i Morral, Nanoscale **7**, 19453 (2015).

[34] M. Fahed, L. Desplanque, D. Troadec, G. Patriarche, and X. Wallart, Nanotechnology **27**, 505301 (2016).

[35] M. Friedl, K. Kristopher Cerveny, P. Weigele, G. Tütüncüoglu, S. Martí-Sánchez, C. Huang, T. Patlatiuk, H. Potts, Z. Sun, M. O. Hill, and L. Güniat, Nano Lett. **18**, 2666 (2018).

[36] See Supplemental Material at http://link.aps.org/supplemental/10.1103/PhysRevMaterials.2.093401 for the following details: Methods; S1, Al deposition; S2, substrate fabrication; S3, InAs SAG on GaAs substrates; S4, GaAs vs GaAs(Sb) buffer growth; S5, thin buffered SAG NW growth; S6, InAs/InP interface; S7, device gating hysteresis; S8, capacitance modeling; S9, field effect mobility fitting; S10, AB oscillation spectral analysis; and S11, WAL fitting procedure.

[37] S. Vaitiekėnas, A. M. Whiticar, M. T. Deng, F. Krizek, J. E. Sestoft, S. Marti-Sanchez, J. Arbiol, P. Krogstrup, L. Caparis, and C. M. Marcus, arXiv:1802.04210.

[38] P. Krogstrup, H. I. Jørgensen, E. Johnson, M. H. Madsen, C. B. Sørensen, A. F. i Morral, M. Aagesen, J. Nygård, and F. Glas, J. Phys. D: Appl. Phys. **46**, 313001 (2013).

[39] E. Ahmad, M. R. Karim, S. B. Hafiz, C. L. Reynolds, Y. Liu, and S. Iyer, Sci. Rep. **7**, 10111 (2017).

[40] W. Sarney, S. Svensson, E. Anderson, A. Lundquist, C. Pearson, and J. Millunchick, J. Cryst. Growth **406**, 8 (2014).

[41] M. W. Larsson, J. B. Wagner, M. Wallin, P. Håkansson, L. E. Fröberg, L. Samuelson, and L. R. Wallenberg, Nanotechnology **18**, 015504 (2006).

[42] S. Yoshida, T. Yokogawa, Y. Imai, S. Kimura, and O. Sakata, Appl. Phys. Lett. **99**, 131909 (2011).

[43] M. de la Mata, C. Magén, P. Caroff, and J. Arbiol, Nano Lett. **14**, 6614 (2014).

[44] M. de la Mata, R. Leturcq, S. R. Plissard, C. Rolland, C. Magén, J. Arbiol, and P. Caroff, Nano Lett. **16**, 825 (2016).

[45] E. Fitzgerald, G. Watson, R. Proano, D. Ast, P. Kirchner, G. Pettit, and J. Woodall, J. Appl. Phys. **65**, 2220 (1989).

[46] Y. Iimura, T. Shiraishi, H. Takasugi, and M. Kawabe, J. Appl. Phys. **61**, 2095 (1987).

[47] T. Van Buuren, M. Weilmeier, I. Athwal, K. Colbow, J. Mackenzie, T. Tiedje, P. Wong, and K. Mitchell, Appl. Phys. Lett. **59**, 464 (1991).

[48] Ö. Gül, D. J. Van Woerkom, I. van Weperen, D. Car, S. R. Plissard, E. P. Bakkers, and L. P. Kouwenhoven, Nanotechnology **26**, 215202 (2015).

[49] A. Savitzky and M. J. E. Golay, Anal. Chem. **36**, 1627 (1964).

[50] F. P. Milliken, S. Washburn, C. P. Umbach, R. B. Laibowitz, and R. A. Webb, Phys. Rev. B **36**, 4465 (1987).

[51] A. E. Hansen, A. Kristensen, S. Pedersen, C. B. Sørensen, and P. E. Lindelof, Phys. Rev. B **64**, 045327 (2001).

[52] J. Dufouleur, L. Veyrat, A. Teichgräber, S. Neuhaus, C. Nowka, S. Hampel, J. Cayssol, J. Schumann, B. Eichler, O. G. Schmidt, B. Büchner, and R. Giraud, Phys. Rev. Lett. **110**, 186806 (2013).

[53] G. Seelig and M. Büttiker, Phys. Rev. B **64**, 245313 (2001).

[54] T. Ludwig and A. D. Mirlin, Phys. Rev. B **69**, 193306 (2004).

[55] F. Pierre, A. B. Gougam, A. Anthore, H. Pothier, D. Esteve, and N. O. Birge, Phys. Rev. B **68**, 085413 (2003).

[56] B. L. Altshuler, A. G. Aronov, and D. E. Khmelnitsky, J. Phys. C: Solid State Phys. **15**, 7367 (1982).

[57] C. Kurdak, A. M. Chang, A. Chin, and T. Y. Chang, Phys. Rev. B **46**, 6846 (1992).

[58] B. L. Al'Tshuler and A. G. Aronov, JETP Lett. **33**, 499 (1981).

[59] A. E. Hansen, M. T. Björk, I. C. Fasth, C. Thelander, and L. Samuelson, Phys. Rev. B **71**, 205328 (2005).

[60] S. Estévez Hernández, M. Akabori, K. Sladek, C. Volk, S. Alagha, H. Hardtdegen, M. G. Pala, N. Demarina, D. Grützmacher, and T. Schäpers, Phys. Rev. B **82**, 235303 (2010).

[61] T. Jespersen, P. Krogstrup, A. Lunde, R. Tanta, T. Kanne, E. Johnson, and J. Nygård, Phys. Rev. B **97**, 041303 (2018).

[62] I. Van Weperen, B. Tarasinski, D. Eeltink, V. S. Pribiag, S. R. Plissard, E. P. A. M. Bakkers, L. P. Kouwenhoven, and M. Wimmer, Phys. Rev. B **91**, 201413 (2015).